

AIAS 2019 International Conference on Stress Analysis

Development and calibration of a CFD-based model of the bed fusion SLM additive manufacturing process aimed at optimising laser parameters

Maria Rita Ridolfi^{a*}, Paolo Folgarait^a, Valerio Battaglia^a, Tiziana Vela^a, Domenico Corapi^a, Andrea Di Schino^b

^a*Seamthesis S.r.l., Piacenza 29122, Italy*

^b*Università di Perugia, Perugia 06123, Italy*

Abstract

The main concern deriving from the Selective Laser Melting technique is attaining a fully dense part out of the interconnected tracks. The right choice of process parameters is of fundamental importance to get a porosity free component. In this work a model has been developed simulating the printing process with the aim of creating a simple numerical tool for designing processing windows suitable to metal alloys of any composition. The applied simplified approach makes the model use as much practical as possible, while keeping the physical description representative. The model has been calibrated fitting experimental measures of track width, depth and cross sectional area taken from three literature sources, referring to: Ti6Al4V, Inconel 625 and Al7050. Effective liquid pool thermal conductivity, laser absorptivity and depth of application of laser energy are the fitting parameters. Laser absorptivity and depth of application of laser energy result to rise almost linearly with increasing specific energy; the slopes of the three analyzed alloys result very close to each other. The obtained results give confidence about the possibility of using the model as a predicting tool after further calibration on a wider range of metal alloys.

© 2019 The Authors. Published by Elsevier B.V.

This is an open access article under the CC BY-NC-ND license (<http://creativecommons.org/licenses/by-nc-nd/4.0/>)

Peer-review under responsibility of the AIAS2019 organizers

Keywords: additive manufacturing; SLM, metal alloys; numerical model; laser parameters; processing window

* Corresponding author. Tel.: +039-06-97858523

E-mail address: mariarita.ridolfi@seamthesis.com

1. Introduction

Selective Laser Melting (SLM) is one of the most widely spread and successful powder bed fusion based additive manufacturing technologies. In SLM melting and solidification of a small volume of powder is achieved using a high intensity laser scanning over a layer of powder. Finally, the part is obtained connecting partially overlapping tracks consolidated over any single layer, with traces previously scanned on a few number of layers below, partially remelted and consolidated.

The main concern deriving from this technique is attaining a fully dense part out of this interconnection of tracks. All the expected mechanical properties of an AM part, such as strength, ductility, creep and fatigue behaviors largely, although not uniquely, depend on the presence of porosities (Mower et al. (2016), Mindt et al. (2018), Gong et al. (2014), Kharallah et al. (2016)). The right choice of process parameters is of fundamental importance to get a porosity-free component, and should be based on powder composition and size distribution. Theoretically, the process parameter list comprises all the following: layer thickness, hatch, laser spot diameter, scanning speed, laser power. Layer thickness comes from considerations about the resolution of the part details and on the target surface finish, while laser spot diameter is often fixed on commercial machines. The optimal process design relies eventually on the right choice of laser power and velocity as well as on hatch distance. Hence, in view of optimizing the SLM process for producing dense part of a given metal alloy, one should have tools to define the operating window in the P - v (laser beam Power – velocity) space, depending on metal alloy composition and powder granulometry.

Beuth et al. (2001) developed the process mapping approach to simply illustrate the process outcomes of an AM process based on input power and velocity. Commonly plotted are curves of constant cross sectional area showing what power and velocity combinations will result in a similar melt pool cross sectional area.

Numerical modeling of the track melting has been approached by the use of commercial finite element software's.

One of these approaches is found in Montgomery et al. (2015), who reports about experiments performed at the National Institute of Standards and Technology (NIST) using an EOSINT M270 Laser Powder Bed system on an IN625 plate. A test matrix of various power and velocity combinations was created, spanning the entire standard operating region of the EOSINT M270 machine. Laser process simulations were performed using a 3D finite element model and the calculated cross sectional areas compared with the measured ones, obtaining not perfect fitting using a fixed value of effective laser absorptivity of 0.57, inducing to hypothesize better fitting for an absorptivity varying with laser power and speed. Almost constant cross sectional area has been found to correspond to linear curves in the laser Power-velocity plane.

The scope of the work described in this paper is creating a modeling tool for generating processing maps of metal alloys applicable to the laser PBF technology, avoiding resorting to experimental testing, as much as possible. To achieve this target a simplified physical frame is modeled to reduce computing time. The model is then applied spanning over the process parameters ranges allowed by the specific AM machine providing as output the limits of the conduction, transition and keyhole modes in the laser Power-velocity plane, along with the full dense region.

Experimental data concerning metal alloys of widely differentiated thermo-physical properties are necessary for the model validation and calibration. Right to this scope, three sources of data have been selected throughout the literature at this first step of the model evolution. The first one is found in the aforementioned paper of Montgomery et al. (2015), while the other two are hereafter described.

Dilip et al. (2017) applied the mapping technique to analyse the variation of melt pool geometry and as-built porosity with laser power and velocity processing alloy Ti6Al4V. Microstructural studies on the melt pool cross-section show that the cross section area increases with increasing laser specific energy. The depth of penetration of the melt pool was observed to increase with increasing the specific energy and in some cases a keyhole effect was observed. The porosity evolution demonstrates a good correlation between the single track melt pool geometry and porosity in the bulk parts. Low energy density and high energy density both result in porosity in the parts due to different reasons being the first one associated to lack of fusion and the second one to porosity generated by the keyhole phenomenon.

Alloy Al7050 melting mode transition and the characteristics between the keyhole and the conduction mode have been investigated by T. Qi et al. (2017), who report about experiments carried on at constant laser power of 200 W. According to the research results, three kinds of melting mode, conduction, transition and keyhole were found,

depending on the process parameters, the melting mode varies from keyhole to conduction with the increase of scanning speed from 100 to 1200 mm·s⁻¹.

2. Background of physical aspects

The continuous metamorphosis of the melt pool at rising specific laser energy is dictated by the onset of gas/melt surface evaporation, occurring when the temperature is high enough. The conduction mode ends up and a recoil momentum (King et al. (2014)) is produced which deforms the initially flat gas/melt interface and forms an increasingly deeper cavity with increasing the laser entering specific energy. As the cavity deepens, much energy get absorbed inside the cavity due to multiple ray reflections against the cavity interface (Maina et al. (2018)). Due to this mechanism, a shallow cavity intercepts less energy than a deep keyhole cavity, resulting in a continuous increase of the effective laser absorbance of the interface achieving its minimum in the conduction mode; afterwards increasing in the transition mode, until reaching the maximum close to unity, for a fully developed keyhole. The absorbance minimum value is strictly correlated to the natural absorptivity of the metal alloy.

Consequently, the melt pool geometry transforms turning from wide and flat into narrow and deep.

3. Model setup

3.1 Model guidelines

The model is developed using the finite volume instead of the more frequently adopted finite element technique to properly account for the gas cooling effect, depending not only on its velocity intensity but also on verse and direction. The effects of gas cooling are not investigated in this work, describing the basic set up and validation of the model and will be object of deeper investigations in the near future.

Aiming at a simplified representation of the welding process, two main assumptions are made.

The first one comes from avoiding evaporation and keyhole formation explicit simulation. Heat transfer is modelled in terms of conduction through the melt pool for any operating condition input. This implies an accurate model validation and calibration for properly taking into account how much evaporation and formation of the cavity affect the melt pool geometry and overall heat transfer conditions.

The second assumption consists in modelling the powder layer as a continuum material, deriving its thermo-physical properties based on local powder particles arrangements, leading to formation of sites where powder is packed or rarefied (as the effect of the mixture with the gas). The aim is that of modelling the effects of the powder density unevenness on the track geometry.

The first applications, herein discussed, refer to single tracks generated over a single powder layer and have been used to calibrate the model using consistent experimental data (Dilip et al. (2017), Montgomery et al. (2015), Qi et al. (2017)).

3.2 Model description

The model has been developed with ANSYS Fluent 17.1. It is based on the solution of the transport equation applied to momentum:

$$\rho \frac{\partial u_i}{\partial t} + \rho \frac{\partial (u_i u_j)}{\partial x_j} = \frac{\partial}{\partial x_i} \left[\mu \left(\frac{\partial u_i}{\partial x_j} + \frac{\partial u_j}{\partial x_i} \right) \right] - \frac{\mu}{K} (u_i - u_i^s) - \frac{\partial p}{\partial x_i} + \rho g_i \quad (1)$$

and energy:

$$\frac{\partial}{\partial t} (\rho H) + \nabla (\rho \vec{u} H) = \nabla (k \nabla T) + S_v \quad (2)$$

The source term (S_v) appearing in the second term of the right hand side of eq. (1) accounts for the Darcy's damping force due to the flow of liquid metal through the mushy zone represented as a porous medium of porosity K , obtained with the Karman-Kozeny equation:

$$K = \frac{PDAS^2}{180} \frac{f_l^3}{(1-f_l^2)+0.001} \quad (3)$$

expressed in terms of the primary arm spacing ($PDAS$) and of the liquid fraction (f_l). The effect of adding this term is negligible for most metal alloys, being the mushy zone extension at such high cooling rates very small. Otherwise, the fluid-dynamics through the mushy zone could affect the thermal field when processing alloys having large solidification intervals.

The energy input coming from the laser beam is given in the last term of the right hand side of eq. (2) in terms of energy per unit volume, following the approach of (Mukerjee et al. (2016)). The method consists in applying the heat input at each time step of the transient analysis to cells enclosed in a virtual cylindrical volume located just below the laser spot. The scheme in Fig. 1 shows the moving laser beam and the volume of the energy application whose expression is given by:

$$S_v = \frac{D\alpha\eta P}{\pi r_l^2 h} e^{-D \frac{x^2+y^2}{r_l^2}} \quad (4)$$

where α is laser absorptivity and η laser efficiency.

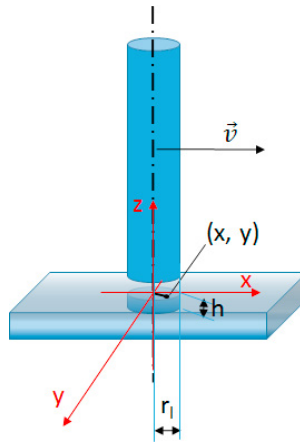


Fig. 1. Scheme showing the ideal cylindrical volume inside which the laser energy source is simulated, moving with the laser beam at velocity v .

The powder bed is simulated as a continuum having density and specific heat calculated as volume fraction weighted average of gas and metal respective properties. Thermal conductivity has given a value lower than what would result from the volume fraction weighted average. A simplified scheme of heat transfer has been introduced, which will be object of further study and refinement. According to the scheme shown in Fig. 2, heat flux exiting from the bead surface, contacting the surrounding powder, is considered to flow out a given fraction of the surface (β), travelling through a first conductive path formed by contacting particles; the heat flows out the remaining surface fraction through a second path crossing few separated particles. The heat crosses these two paths in parallel. At the present stage, some particle arrangements in the two paths, consistent with the powder bed gas fraction, led to estimate an effective thermal conductivity about 12÷14 % of the metal conductivity, depending on the gas composition. This approach is designed to allow for future analyses of effects due to powder rarefactions or agglomerations, provided its specific calibration.

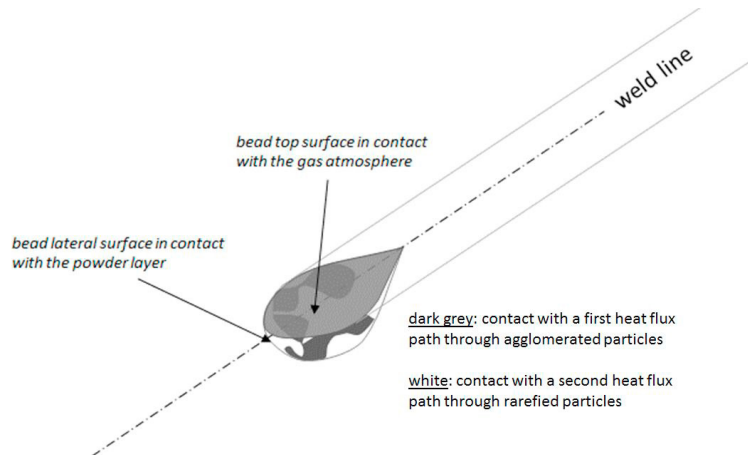


Fig. 2. Scheme showing the bead surface in contact with the powder layer and its subdivision into regions contacting full metal and full gas.

The simulation domain consists of a parallelepiped including: platform, one powder layer and gas atmosphere. Only one half of the track is simulated for symmetry reasons, cut with a vertical longitudinal plane. All the other boundaries are given adiabatic conditions and zero velocity. Sensitivity analyses on the cell size and total transient time of simulation have been performed to ensure that the results do not vary with further decreasing the cell size and that regime temperature field is attained. A mesh adapting scheme has been applied, based on local temperature, in order to refine only the hotter region of the domain. Finally, cell size as small as $3\ \mu\text{m}$ has been employed and the transient time of simulation has been assessed as to provide a 1 mm long track, depending on the scanning speed.

4. Model calibration

The model has been calibrated fitting experimental measures of track width and depth taken from Dilip et al. (2017), Montgomery et al. (2015), Qi et al. (2017).

Dilip et al. (2017) reports about single tracks fabricated at four laser powers between 50 W and 195 W and four velocities between $500\ \text{mm s}^{-1}$ and $1200\ \text{mm s}^{-1}$. Laser scans are made with an EOSINT M270 Laser Powder Bed system, using a single Ti6Al4V powder bed layer, $30\ \mu\text{m}$ thick, deposited over a Ti6Al4V platform. Track width and depth measures are available for all tested power and velocity combinations for model fitting.

Montgomery et al. (2015) performed experiments using an EOSINT M270 Laser Powder Bed system, at seven powers between 50 W and 195 W and six velocities between $200\ \text{mm s}^{-1}$ and $1200\ \text{mm s}^{-1}$. One powder layer, $20\ \mu\text{m}$ thick is put over the platform. Transverse track section area measures here reported have been used for fitting the present model.

Qi et al. (2017) used a self-developed SLM system for their experiments consisting in fabricating single tracks at 200 W and increasing velocity from $100\ \text{mm s}^{-1}$ up to $1200\ \text{mm s}^{-1}$, for a total of thirteen velocities, using a single powder layer of thickness $20\ \mu\text{m}$. Values of width and depth are available for the current model purpose.

The strategy applied to gain fitting results involves two different stages. In the first stage, the input laser specific energy is raised from the lowest level, the height h is set to an initial value and the laser absorptivity is given as first attempt the value competing to the simulated metal alloy, as deduced from available databases of metal surfaces reflectivity. Both h and α keep constant values for all operating conditions resulting in conduction mode.

The calibration when simulating the conduction mode is addressed at fitting measured depth and width data and at obtaining the boiling conditions in the weld pool at operating conditions experimentally marking the passage from conduction to evaporation. Experimental data employed in this work provide numerous track measures at different P - v values, scanning over the operating ranges of P and v with quite fine resolution, allowing for precisely detecting the transition from conduction to evaporation and keyhole formation. Laser absorptivity and effective thermal conductivity in the liquid pool are set as fitting parameters. Up to now, the calibration experience shows almost no need to vary the laser absorptivity derived from literature and web repositories referring to each metal alloy.

In the second stage, height h and α are varied with varying laser parameters until fitting measured values of depth and width. In particular, absorptivity increases with increasing the input laser specific energy until reaching a plateau at a value close to unity. Laser efficiency η has been kept constant and equal to 0.85.

Table 1 resumes the main thermo-physical parameters for the three alloys.

Table 1. Thermo-physical properties of the three alloys used for the model calibration.

Metal alloy	Ti6Al4V	INC625	Al7050
Density (kg m^{-3})	4000	8440	2810
Liquidus temperature: T_{liq} (K)	1986	1607	906
Solidus temperature: T_{sol} (K)	1970	1513	787
Specific heat ($\text{J kg}^{-1} \text{K}^{-1}$)			
ambient temperature	550	440	860
T_{sol}	830	650	1050
T_{liq}	980	670	1120
Thermal conductivity ($\text{W m}^{-1} \text{K}^{-1}$)			
ambient temperature	5	11	117
T_{sol}	32	30	156
T_{liq}	32	30	87
$T > T_{liq}$	96	90	148
Latent heat of fusion (J m^{-3})	$1.4 \cdot 10^9$	$1.99 \cdot 10^9$	$1.05 \cdot 10^9$
Boiling temperature (K)	3560	3003	2793
Reflectivity at $1.06 \mu\text{m}$	0.52	0.71	0.65

5. Results

The comparison between measured and calculated cross sectional data are shown in Fig. 3, in terms of width and depth data concerning the analysis performed on Ti6Al4V (Dilip et al. (2017)) and Al7050 (Qi et al. (2017)), respectively in Fig 3 (a) and (c), and of cross sectional area for Inconel 625 (Montgomery et al. (2015)) in Fig. 3 (b).

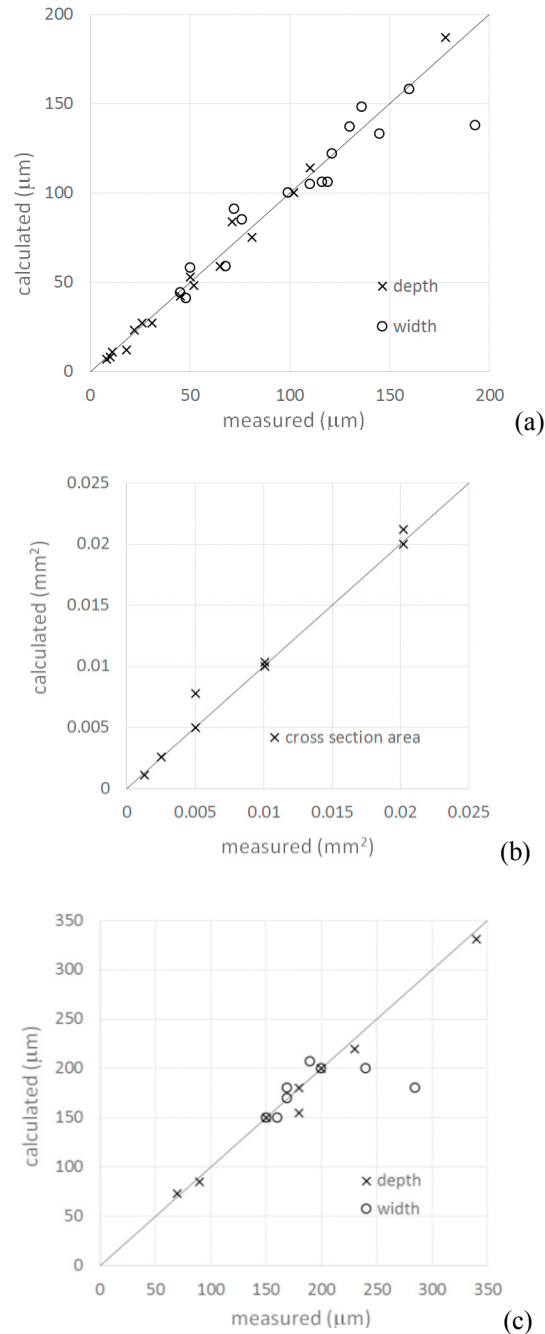


Fig. 3. Comparison between measured and calculated data of:
 (a) Ti6Al4V track depth and width from Dilip et al. (2017)
 (b) Inconel 625 track cross section area from Montgomery et al. (2015)
 (c) Al7050 track depth and width from Qi et al. (2017).

An average good match has been found with exception of width values for deep keyhole shapes. The typical keyhole cross section geometry is characterised by a width profile rapidly changing from wide, near the surface, to narrow deep below. The simplified approach of the present model is not capable to catch this geometry complexity.

The net result is that it fails in giving precise width values, although calculated depth and cross sectional area fit well the measured values.

The fitting parameters: h and α shows the trends against specific energy, shown respectively in Fig. 4 and 5.

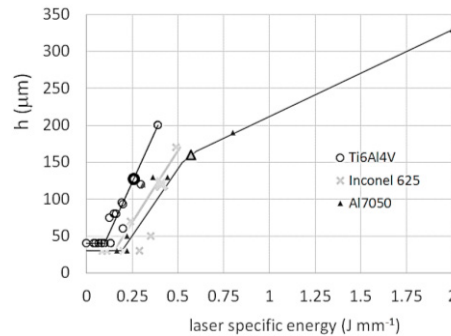


Fig. 4. Calculated trends of height h vs specific energy for the three analysed alloys.

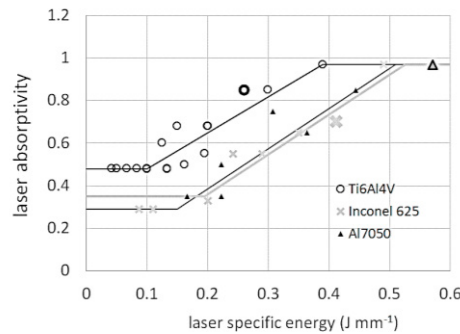


Fig. 5. Calculated trends of laser absorptivity vs specific energy for the three analysed alloys.

Bold symbols in Fig. 4 and 5 highlight specific energies above which deep keyhole is experimentally observed for the three alloys. Dilip et al. (2017) put into evidence presence of keyhole porosity for specific energies above 0.26 J mm^{-1} . Montgomery et al. (2015) clearly notice keyhole shape for specific energies above 0.4 J mm^{-1} and Qi et al. (2017) recognise well developed keyhole regime only at very high power level, close to 2 J mm^{-1} , although severe keyholing is detected at specific energy as low as 0.57 J mm^{-1} .

While for Ti6Al4V and Inconel 625 this experimental outcome meet the respective calculated curves at $\alpha \approx 0.8$, the keyhole observed in Al7050 tracks appears for a calculated $\alpha = 0.97$.

6. Observations and future needs

The described analyses show that the simplified model allows the prediction of track geometry, welding mode, deep keyhole formation, provided that correct input is given in terms of: metal pool effective thermal conductivity, trends of h and α vs specific energy, at specific energies for which the pool temperature overcome the boiling point. The increase of effective liquid thermal conductivity can be associated to the intense convection occurring in the real liquid pool, due to thermal convection and surface tension effects, which are not properly accounted for by the model, due to the way heat is input and to the absence of surface tension modelling.

Indications derived from the present work show that a correlation between the effective liquid pool conductivity and the real one can be found. Introducing the multiplying factor, C_k , the effective conductivity, k_{eff} , can be expressed as C_k times the real liquid conductivity. Tracing on a graph the values of C_k emerging from the calibration, the curve of Fig. 6 is interpolated as first attempt, having an asymptotical trend to unity for indefinitely increasing conductivity. Roughly, the curve in Fig. 6 leads to the trivial conclusion that effective conductivity is

increased by thermal convection, much more when the liquid conductivity is low (higher gradients in the liquid pool), than when it is high (flat temperature field).

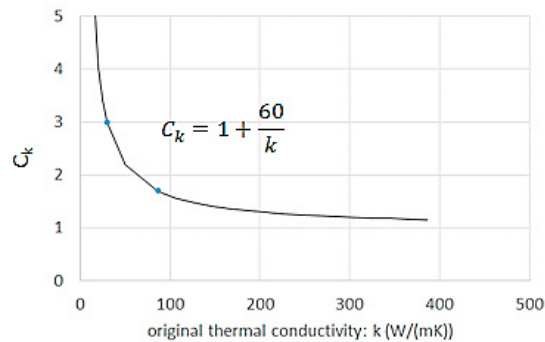


Fig. 6. Trend of multiplying coefficient C_k with real liquid conductivity of the alloy, for the effective liquid conductivity calculation.

The curves of h and α shown in Fig. 4 and 5, show very similar slope for the three alloys. Only for Al7050, operating conditions leading to very deep tracks have been experienced, giving the possibility of observing how the continuous rise of the penetration depth due to the drilling action of the plume, is slowed down after reaching the maximum absorbance of laser power. Otherwise, operating conditions of deep keyhole are not of industrial interest due to the connected high risk of porosity. The results obtained until now show an almost linear increasing trend for both h and α until reaching conditions of deep keyhole.

Both C_k and the slopes of h and α need to be adequately verified and modified through calibrations to be performed on other alloys. Eventually, they could result to be in good correlation with alloy thermo-physical properties, releasing as much as possible the model from the use of empirical parameters.

In the future the model will be implemented with the calculation of the component density, coming from the calculated track geometry, layer thickness and track hatch, obtaining the residual porosity due to not completely fused powder. On the other hand, reaching the level of absorptivity competing to deep keyhole will give a rough measure of the risk of porosity due to gas entrapped at the bottom of the keyhole cavity.

7. Conclusions

A model has been developed using the commercial code ANSYS Fluent for simulating the printing process inside a SLM machine. A simplified approach has been adopted to make the model use as much practical as possible for design the processing window of alloys of any composition.

The model has been calibrated fitting experimental measures of track width, depth and cross sectional area taken from three literature sources, referring to: Ti6Al4V, Inconel 625 and Al7050.

A strategy of model calibration is employed based on varying the effective liquid pool thermal conductivity in order to fit the experimentally observed evaporation start with the calculation of the boiling temperature as maximum pool temperature. Laser absorptivity and depth of application of laser energy are further varied in order to fit width and depth data. They result to rise almost linearly with increasing specific energy assuming slopes very close for the three analyzed alloys. In particular, laser absorptivity increase from the base level consistent with the absorptivity of the alloy at the laser wavelength, until reaching a maximum value close to unity. From the experiments described in the reference papers used in this work, deep keyhole already appears for calculated values of absorptivity of almost 0.8.

The model needs to be further calibrated to validate the present observations and refine the fitting parameters (effective liquid conductivity, slope of h and α).

In its future use, the calibrated model is conceived as a tool for predicting the welding mode at given power and velocity (process window), the component density deriving from uncomplete powder melting and the risk of keyhole porosity.

Nomenclature

C_k	multiplying factor
D	distribution factor
f_l	metal liquid fraction in the mushy zone
g_i	gravity acceleration components (m s^{-2})
h	height of the cylinder of laser heat application
H	enthalpy (J kg^{-1})
k_{eff}	effective thermal conductivity ($\text{W m}^{-1} \text{K}^{-1}$)
K	mushy zone permeability (m^2)
p	pressure (Pa)
P	laser power (W)
PDAS	primary dendrite arm spacing (m)
r_l	laser beam radius
S_v	volumetric heat source (J m^3)
T	time (s)
T_{liq}	liquidus temperature (K)
T_{sol}	solidus temperature (K)
u_i, u_j	velocity components (m s^{-1})
v	scanning speed (m s^{-1})
x, y	coordinates in a frame relative to the laser beam (m)
x_i, x_j	coordinates (m)
α	laser absorptivity
β	fraction of the track surface contacting powder
η	laser efficiency
μ	viscosity (Pa s)
ρ	density (kg m^3)

Acknowledgements

The authors acknowledge the support and active contribution given by an important society operating in the field of industrial gases for the development of the model.

References

- Beuth, J., Klingbeil, N., 2001. The Role of Process Variables in Laser-Based Direct Metal Solid Freeform Fabrication, JOM 53, no. 9, 36-39.
- Dilip, J., J., S., Zhang, S., Teng, C., Zeng, K., Robinson, C., Pal, D., Stucker, B., 2017. Influence of processing parameters on the evolution of melt pool, porosity, and microstructures in Ti-6Al-4V alloy parts fabricated by selective laser melting, Progress in Additive Manufacturing 2, no. 3, 157–167.
- Gong, H., Rafi, K., Gu, H., Stucker, T., S., B., 2014, Analysis of defect generation in Ti–6Al–4V parts made using powder bed fusion additive manufacturing processes, Additive Manufacturing 1-4, 87-98.
- Khairallah, S., A., Anderson, A., T., Wayne, A., R., King, E., 2016, Laser powder-bed fusion additive manufacturing: Physics of complex melt flow and formation mechanisms of pores, spatter, and denudation zones, Acta Materialia 108, 36-45.
- King, W., E., Barth, H., D., Castillo, V., M., Gallegos, G., F., Gibbs, J., W., Hahn, D., E., Kamath, C., Rubenchik, A., M., 2014. Observation of keyhole-mode laser melting in laser powder-bed fusion additive manufacturing, Journal of Materials Processing Technology 214, 2915–2925.
- Maina, M., R., Okamoto, Y., Inoue, R., Nakashiba, S., Okada, A., Sakagawa, T., 2018. Influence of Surface State in Micro-Welding of Copper by Nd:YAG Laser, Appl. Sci. 8, no. 2364, 1-13.

- Mindt, H.-W., Desmaison, O., Megahed, M., Peralta, A., Neumann, J., 2018, Modeling of Powder Bed Manufacturing Defects, *Journal of Materials Engineering and Performance* 27, no. 1, 23–43.
- Montgomery, C., Beuth, J., Sheridan, L., Klingbeil, N., 2015. Process Mapping of Inconel 625 in Laser Powder Bed Additive Manufacturing, *Proceedings of the Annual International Solid Freeform Fabrication Symposium*, 1195–1204.
- Mower, T., M., Long, M., J., 2016. Mechanical behaviour of additive manufactured, powder-bed laser-fused materials, *Materials Science and Engineering: A* 651, 198–213.
- Mukherjee, T., Zuback, J., S., De, A., DebRoy, T., 2016. Heat and fluid flow modeling to examine 3d printability of alloys, *7th International Symposium on High-Temperature Metallurgical Processing*, 471–478.
- Qi, T., Zhu, H., Zhang, H., Yin, J., Ke, L., Zeng, X., 2017. Selective laser melting of Al7050 powder: Melting mode transition and comparison of the characteristics between the keyhole and conduction mode, *Materials & Design*, doi: 10.1016/j.matdes.2017.09.014.